Understanding detrimental and beneficial grain boundary effects in halide perovskites

Gede W.P. Adhyaksa[1], Sarah Brittman[1,2], Haralds Āboliņš[1], Andries Lof[1], Xueying Li[3], Joel D. Keelor[4], Yanqi Luo[3], Teodor Duevski[1], Ron M.A. Heeren[4], Shane R. Ellis[4], David P. Fenning[3], Erik C. Garnett[1]*

[1]Center for Nanophotonics, AMOLF, Science Park 104, 1098 XG Amsterdam, The Netherlands
[2]Current address: U.S. Naval Research Laboratory, 4555 Overlook Avenue SW, Washington, D.C. 20375, USA
[3]Department of Nanoengineering, University of California San Diego, CA 92093, USA
[4]The Maastricht Multimodal Molecular Imaging Institute (M4I), Division of Imaging Mass Spectrometry, Maastricht University, 6229 ER Maastricht, The Netherlands
*e.garnett@amolf.nl

Abstract

Grain boundaries play a key role in the performance of thin-film optoelectronic devices and yet their effect in halide perovskite materials is still not understood. The biggest factor limiting progress is the inability to identify grain boundaries. Non-crystallographic techniques can misidentify grain boundaries, leading to conflicting literature reports about their influence; however, the gold standard – electron backscattering diffraction (EBSD) – destroys halide perovskite thin films. Here we solve this problem by using a solid-state EBSD detector with 6,000 times higher sensitivity than the traditional phosphor screen and camera. Correlating true grain size with PL lifetime, carrier diffusion length and mobility, shows that grain boundaries are not benign but have a recombination velocity of 1670 cm/s, comparable to that of crystalline silicon. We also observe amorphous grain boundaries that give rise to locally brighter photoluminescence intensity and longer lifetimes. This anomalous grain boundary character offers a possible explanation for the mysteriously long lifetime and record efficiency achieved in small grain halide perovskite thin films. It also suggests a new approach for passivating grain

boundaries, independent of surface passivation, to lead to even better performance in optoelectronic devices.

Keywords

Halide perovskite, amorphous grain boundary, grain size effect, electron backscatter diffraction (EBSD), carrier lifetime, diffusion length, mobility.

Introduction

Minimizing non-radiative recombination is critical to achieving high efficiencies in optoelectronic devices. Halide perovskites are an emerging class of semiconductors whose optoelectronic properties are tolerant to defects[1,2], relative to conventional semiconductors. Although the trap density in polycrystalline perovskite films is typically 10^{14} - 10^{16} cm^{-3} (as high as fifty per million unit cells)[3,4], their photovoltaic power-conversion efficiencies exceed 20%[5]. Single-crystalline perovskites exhibit far lower trap densities (as low as 10^{10} cm^{-3})[6], and this difference indicates that polycrystalline thin films possess additional sources of non-radiative recombination such as more bulk defects, less well-passivated surfaces, or grain boundaries.

To improve the efficiency of devices made from polycrystalline perovskites, it is necessary to push the trap density of these films to lower values, toward those reported for single crystals. To achieve this, we first must understand which of these sources of non-radiative recombination is most important to reduce, a task that is complicated by the conflicting reports regarding whether grain boundaries in halide perovskite films are beneficial or detrimental[7-9]. Several studies[10-15] on $CH_3NH_3PbI_3$ perovskite films with grain boundaries less than 5 μm show that carrier lifetime, mobility, and diffusion length increase with grain size, as does the power conversion efficiency of solar cells. These correlations suggest that grain boundaries contribute to non-radiative recombination and reduce device performance. Improvements in performance have also been reported for films with grain size even up to the millimeter-scale [16]. In contrast, Kelvin probe force microscopy studies of $CH_3NH_3PbI_3$ films have shown that grain boundaries are beneficial for charge separation and collection[7], and theory has suggested that PbI_2 at grain boundaries can be beneficial,[17] supporting an earlier hypothesis[18,19]. Furthermore, experiments examining the effects of grains on photovoltaic performance have indicated that heterogeneity of local voltage[20] and crystal facets[21] near grain boundaries are important factors.

All of these studies on perovskite films have inferred the grain size and grain boundary locations based on optical or scanning electron microscope (SEM) images, which contain no crystallographic information. Therefore, the first step toward understanding the complex effects of grain boundaries is quantifying their local crystallographic metrics. Traditionally, electron backscatter diffraction (EBSD) is the gold standard for measuring grain size, orientation and boundary location in thin film samples. However, its use in halide perovskites has been hampered by beam-induced damage, making EBSD mapping impossible in thin film samples so far. There has been one report of single spot EBSD measurements, which was limited to single crystals where grain boundaries cannot be studied.[22]

Here we use a new type of solid-state EBSD detector with 6,000 times higher sensitivity than the traditional camera and phosphor screen to collect EBSD maps of grain size and orientation in $CH_3NH_3PbBr_3$ thin films. We developed a thin film deposition protocol that allows us to control the resulting average grain size over a large range between 1 and 60 microns. We show that the average grain size measured from EBSD is different (up to a factor of ~1.9) from what is inferred from optical and SEM images. Furthermore, we correlate the accurate values with photoluminescence intensity and lifetime, minority carrier diffusion length, and mobility. Larger grain size (even up to 60 microns) is generally beneficial for all properties. Although most samples show crystalline grain boundaries, samples with amorphous regions at the grain boundaries show properties better than expected according to their grain size. The longer PL lifetime and higher PL intensity at these amorphous regions suggests that amorphous interfaces can improve optoelectronic properties, perhaps either by improving grain boundary passivation or gettering native defects. Putting the grain size dependence of optoelectronic properties into a recombination model shows that grain boundary recombination plays an important role in the maximum achievable solar cell and LED efficiency up to grain sizes approaching a millimeter.

Results

Grain size control and grain boundary determination

In order to systematically study grain boundary effects, we used a deposition procedure that produces continuous and highly oriented films of $CH_3NH_3PbBr_3$[23]. We dissolve $Pb(CH_3COO)_2 \cdot 3H_2O$ and CH_3NH_3Br in dimethylsulfoxide (DMSO) in a 3.05:1 ratio. Changing only the spincoating time allows us to tune the grain size over a range of 1-60 microns by

controlling the nucleation density of an intermediate phase that converts to perovskite upon annealing (details in supplementary note 1, **Figure S1-S3**).[24-27] This method successfully decouples the nucleation and growth steps of the film and therefore offers control over its final grain size on a variety of substrates such as glass, silicon, TiO_2, and ITO (**Figure S4**).

We carried out EBSD measurements in an electron microscope that was equipped with a solid-state detector initially designed as a position sensitive, single photon counting detector, from which other applications such as ion and electron detection have evolved (**Figure 1a**).[28,29] The sensor is equipped with an electronic noise free circuit, and therefore provides high sensitivity and fast readout, which enable us to acquire clear EBSD maps of halide perovskite films on glass quickly before damaging the samples. We used an optimized beam current of 100 pA at an accelerating voltage of 30 kV, with a pixel dwell time of 100 ms. The electron dose needed for acquiring EBSD maps here is 6,000 times lower than what was previously necessary for single crystal samples using the traditional phosphor screen and camera (6nA for 10 s)[22]. Back-scattered electrons escape from the tilted sample and are projected onto the detector in a pattern of spherical bands that reflect the Bragg angles of the local crystal lattice (Kikuchi lines)[30]. By scanning the beam across the sample, we collected a pattern from each pixel and indexed it to the cubic $CH_3NH_3PbBr_3$ lattice to construct a map of the film's local crystallographic orientations.

Figure 1b-e shows EBSD maps of the $CH_3NH_3PbBr_3$ perovskite prepared with different spinning times. The grain size becomes larger with reduced spinning time (at a given spin speed), which is consistent with trends inferred from SEM (top panel **Figure 1b-e**). Most crystal grains are oriented in the [001] direction and the surface orientation propagates throughout the whole film (**Figure S10**). On samples with larger than average grain size, however, the population becomes more dispersed to higher index orientations of [101] and [111]) because of many smaller crystal grains trapped among adjacent larger grains (bottom panel **Figure 1b-e**). The mean of the distribution of apparent grain sizes obtained from optical images differs from the mean of the distribution obtained using EBSD (**Figure 1g**, the method in **Figure S5**). Typically the difference is less than 40%, but in one particular case (orange trace), the optical images indicate an average grain size of more than a factor of 1.9 larger than the actual grain size. **Figure 1f** shows the origins of this discrepancy between an SEM image and its corresponding EBSD map. Some pixels of the map show no Kikuchi pattern, for instance area **4**;

this indicates a disordered region, which could contain amorphous (not fully crystallized) material[31], nanocrystalline perovskite with grains much smaller than our interaction volume (~250 nm based on Monte Carlo simulation; **Figure S6**) or a composite of the two. From EBSD data alone, we also cannot rule out the influence of surface roughness (**Figure S9**). The observation of disordered regions occurs primarily in the sample with an average grain size of 32 μm. In the optical image, such regions would be incorrectly classified as part of their neighboring grains. Furthermore, the identical Kikuchi patterns between domain **1** and **2** in **Figure 1f** (across the dashed line) indicate that they are one grain, while their morphology (based on the SEM) suggests there is a grain boundary. In another area (solid line in **Figure 1f**), the SEM suggests there is no grain boundary but the EBSD map shows that one is present.

To further resolve the origins of the disordered region at the grain boundary, we carried out synchrotron-based nanoprobe X-ray diffraction (nano-XRD) on the sample with <32 μm> grain size (details in supplementary note 3, **Figure S11**). On the basis of the nano-XRD analysis, where no scattering is detected at the grain boundary, the disordered grain boundary regions appear to be amorphous. **Figure 1h** shows a region of grain boundaries where we detected neither scattering from oriented perovskite [001], nanocrystalline perovskite phase, intermediate phase, nor precursor traces of $PbBr_2$. Our nano-XRD scattering geometry was set to detect [001] scattering, but since other orientations such as [101] or [111] can be easily indexed from the EBSD maps (on smooth surfaces), we believe that the disordered regions at the grain boundaries where we detect neither EBSD nor nano-diffraction intensity are amorphous.

Little is known about the crystallographic nature of grain boundaries in halide perovskites; however, thermodynamically the main characteristics of grain boundaries can be inferred by their crystallographic misorientation angles which can be acquired from the EBSD[32-35]. Using crystallographic misorientation angles, we can calculate the interfacial energy among adjacent grain boundaries (details in supplementary note 2, and **Figure S7**). For [001] crystal orientation (83% of the $CH_3NH_3PbBr_3$ perovskite film studied here), the grain boundary interfacial energy increases with crystal misorientation angle up to 14°, but then fluctuates without a pronounced global minimum for samples with both the small (<4 μm>) and large (<54 μm>) grain size (**Figure 1i**). A pronounced global minimum surface energy at high misorientation angle is typically associated with a special boundary, called coherent twinning (e.g. Σ3 or Σ5) which is often observed in other photovoltaic semiconductor materials (CdTe,

chalcopyrite, InP, GaAs, and mc-Si)[36-40]. Removing twinning defects has been shown to improve solar cell performance[39,40]. Although such twinning was previously found on $CsPbX_3$ (X = Cl, Br, I) perovskite nanocrystals[41], and $CH_3NH_3PbI_3$ thin film[42], we have not been able to observe it here, even within a smaller spatial resolution of our large-area EBSD mapping (16 nm resolution, 100 nm stepsize, **Figure S9**), or on the higher index crystal orientation [101] and [111]. In mc-Si for example, the desire to avoid generation of recombination-active intragranular defects such as dislocations and twins has led to a recent trend of reduced grain sizes to improve solar cell performance[43-49]. In contrast, the absence of twinning itself in our films indicates that higher excess interfacial energy at the grain boundary is always induced in order to equilibrate any general structural dislocation (further details of the consequence in supplementary note 2, **Figure S8**).

Grain boundary effects on photoluminescence

To understand how the grain boundaries in $CH_3NH_3PbBr_3$ perovskite films affect photo-generated charge carriers, we recorded photoluminescence (PL) decay profiles on samples each having a different grain size distribution (**Figure 2**). The PL peak was at 534 nm, which is typical for $CH_3NH_3PbBr_3$ perovskite, and the integrated intensity between 475-600 nm was used for the lifetime curves. **Figure 2** shows that when the PL signal, measured locally, is averaged over the entire map, samples with larger grains yield higher PL intensity and longer lifetimes. In the sample with the largest grains, the apparent grain boundaries appear dark (particularly in the lifetime map), which is consistent with their role as a source of non-radiative recombination and would explain the general trend of longer lifetimes in films with larger grains (further discussion regarding the evolution of recombination coefficients, and the effect of diffusion is in the supporting note 4). Unexpectedly, however, the sample with medium-sized grains (**Figure 2b**) shows PL intensity 30 times brighter and lifetimes 3 times longer at the apparent boundaries as compared to the center of the grain. Using wide-field illumination under a wide-range of excitation (10^{16} to 10^{18} cm^{-3}) does not alter this increased PL lifetime near the apparent grain boundaries, and therefore indicates that carrier diffusion outside of the collection spot or wave-guiding effects are not responsible for this effect (details in Supplementary note 4, **Figure S13-S14**)[13,50,51]. Furthermore, by analyzing the local PL intensity as a function of carrier density both near the apparent boundaries and in the center of grains, we confirmed that local variations in

doping are also not responsible for the difference in PL intensity (Supplementary note 4, subsection local doping effect, **Figure S15**). EBSD maps together with nano-XRD analysis indicate that these grain boundaries consist of an amorphous phase (**Figure 1h**). Secondary ion mass spectroscopy (SIMS) maps taken with 192 nm pixel size and x-ray photoelectron spectroscopy (XPS) analysis suggest that the bulk and surface composition of the sample with amorphous boundaries do not differ compared to the other samples with crystalline boundaries. There are some local compositional variations that are similar across all films, but these variations do not correlate with the spatial variations in the PL lifetime or intensity (details in Supplementary note 7, and 8, **Figure S19**, and **S20**). Interestingly, the qualitatively different nature of such an amorphous phase at grain boundaries could explain the mysteriously long lifetimes, large local variations and excellent efficiency seen in some small grain halide perovskite thin-film devices. Furthermore, known chemical passivation treatments might also be creating amorphous regions or surface layers that could account for some of their effectiveness[8, 72]. Our measurements show that the amorphous phase has higher PL intensity and lifetime than the bulk perovskite; however, the longer lifetime does not necessarily indicate improved photovoltaic performance, which depends on the charge carrier diffusion length that is a function of both carrier lifetime and mobility[52].

Grain boundary effects on carrier diffusion lengths

To understand the role of grain boundaries in halide perovskites on electronic transport, we used the steady-state photocarrier grating (SSPG) technique to measure the ambipolar charge-carrier diffusion length within the films[12,53]. This technique relies on measuring lateral carrier transport in the film in the presence of sinusoidal laser interference (an optical grating) created by two monochromatic lasers (450 nm excitation wavelength) where one laser is weaker than the other. Any carrier diffusion length longer than the interference periodicity will smear out the grating's amplitude, and therefore the sample's conductivity can be measured. By monitoring how the sample's conductivity changes as a function of the period of the grating, the minority carrier diffusion length can be extracted (details in supplementary note 5)[54,55]. Using a similar laser excitation wavelength for the SSPG and PL measurements (480 nm), we expect the distribution of the photo-generated carriers to be similar, given that all the films have similar background carrier concentration (Supplementary note 5 and **Figure S18**). We carried out the

measurement on the same samples used earlier for the PL studies and observed that the minority carrier diffusion length increases with grain size (**Figure S17**). The diffusion lengths extracted range from 168 nm to 548 nm with increasing grain size from <4 μm> to <54 μm>. This data clearly shows that the increased grain size still improves the lateral carrier transport, even if the grain size is two orders of magnitude larger than the diffusion length.

Statistical correlation of grain sizes and optoelectronic properties

Generally we observed that $CH_3NH_3PbBr_3$ perovskite films with larger grains yield longer PL lifetimes; however, PL lifetimes for the <32 μm> grained film were longer than expected (**Figure 2 and Figure S13 at variable excitation intensity)**. For each sample, we collected approximately 20 maps of PL lifetime, each from a different spot, and tabulated the trap-assisted (monomolecular) lifetime as a function of grain size in **Figure 3a**. Each data point represents an ~80 x 80 μm^2 PL lifetime map. We find that the mean PL lifetime (see the distribution on the right y-axis, **Figure 3a**) of the <32 μm>-grain sample is longer than that of the <54 μm>-grain sample, even under wide-field illumination (**Figure S14**), which suggests that the grain boundaries in the <32 μm> sample have a different electronic character than those in the other samples. This special electronic character is consistent with the amorphous nature of the grain boundary. **Figure 3b** shows that the diffusion length increases with grain size. The absence of the anomaly at <32 μm> grain sample suggests that the increase in PL lifetime is coupled to a decrease in carrier mobility.

To quantify this relationship, we used Fourier decomposition to solve the steady-state diffusion equation and fit this analytical solution to the data (details in supplementary note 6). We modelled and fit the data numerically; however to obtain an intuitive picture, we can approximate the dependence of carrier diffusion length on grain size by examining the first term in a truncated Fourier expansion[56-64]:

$$L_d = \left(\frac{2S_{GB}}{DG} + \frac{1}{(LA)^2}\right)^{-1/2} \quad (1)$$

where L_d is the minority carrier diffusion length (value that is obtained from the SSPG measurement), S_{GB} is grain boundary recombination velocity, D is the asymptotic value of the

diffusion coefficient of the polycrystalline thin film, G is the grain size, L is the asymptotic value of the diffusion length of the polycrystalline thin film, and A is defined as:

$$A = \frac{1 + \frac{S_{FB}L}{D} tanh\left(\frac{W}{L}\right)}{\frac{S_{FB}L}{D} + tanh\left(\frac{W}{L}\right)} \quad (2)$$

where S_{FB} is front or back surface recombination velocity (assumed to be the same), and W is film thickness. G, L, D, L_d and W are known from the experiments, whereas S_{GB} and S_{FB} were used as free fitting parameters. The values of L and D depend on the quality of the bulk perovskite material and are the asymptotic values of the experimental data for L_d and D calculated using the Einstein relation and the asymptotic effective mobility (μ_{eff}) at which the effect of grain boundaries is no longer relevant (**Figure 3b-c**). After global optimization, we find the solutions for S_{GB}, S_{FB}, L, and D in our sample are 1670 ± 50 cm/s, 27 ± 1.5 cm/s, 0.61 μm, and 0.18 cm^2/s, respectively. Note that with a surface recombination velocity (S_{FB}) 30 times lower than the grain boundary recombination velocity (S_{GB}), grain boundaries still play a significant role in transport up to a grain size of ~20 μm (~35% contribution to L_d). For larger grains, the surface recombination then becomes more influential. Grain boundary recombination accounts for 80% of the reduced L_d when the ratio W/L is 1 (perovskite thickness of 610 nm); much smaller values for W/L (less than ~0.01) are needed before surface recombination dominates. The grain boundary recombination velocity in our polycrystalline $CH_3NH_3PbBr_3$ film is comparable to the surface recombination velocity of single crystalline $CH_3NH_3PbBr_3$ reported by Yang et al.[65] The recombination velocity at the grain boundary for a halide perovskite has not been reported before, but the values obtained here fall around an order of magnitude higher than that of unpassivated CdTe[66] and similar to passivated mc-Si[67,68] or CIGS[69,70].

We can calculate an effective mobility indirectly from the diffusion length measurement (**Figure 3b**) and the PL lifetime data (**Figure 3a**). We find that, except for the <32 μm>-grain sample, the effective mobility increases with grain size (**Figure 3c**); a similar trend was previously reported for $CH_3NH_3PbI_3$ films[10]. In the <32 μm> grain-sample, the amorphous grain boundaries appear to limit mobility because this sample's diffusion length is unchanged, while its lifetimes are anomalously long. The mobility in our $CH_3NH_3PbBr_3$ samples ranges between ~1.5 to 7.5 cm^2/V.s, similar to the values estimated from PL quenching measurements[71]. The

effective mobility presented here is the intrinsic ambipolar transport mobility which will be dominated by the excess carrier with shorter diffusion length (details in Supplementary note 5 and Table S2), thus isolating any effect from transporting layers.

Implications for perovskite thin films, solar cells, and future research

Understanding the role of grain boundaries in perovskite solar cells is essential to push these devices to their peak performance. As a first approximation, grain boundary effects in halide perovskite films have been neglected when the grain size is much larger than the film thickness[16] and all grain boundaries have been treated as having the same effect on performance. In halide perovskite films with grain sizes comparable to the film thickness (less than 1 μm) some studies have reported that grain boundaries reduce mobility[10], diffusion length[12], and solar cell performance[11], but they did not use a crystallographic technique to measure grain size. Such work led to more recent attempts to passivate surfaces and grain boundaries to improve device performance[72-74]. Until now, grain boundary passivation studies have focused on chemical passivation, but without studying the crystallographic nature of the grain boundaries, it is not possible to exclude crystallographic rather than chemical effects. In fact, our study showing highly disordered (likely amorphous) material at some grain boundaries with anomalously high PL intensity and lifetime suggests that chemical passivation may not be the only contributing factor. It is therefore valuable to revisit current chemical grain boundary passivation studies to see if there are any crystallographic changes in the films induced by the use of additives intended for passivation. In this report, we provide a more detailed view of grain boundaries. We have shown in a $CH_3NH_3PbBr_3$ system made from a lead-acetate precursor that grain boundaries still play a dominant role in the optoelectronic properties up to the range of <20 μm>, after which surface recombination dominates. We also show that crystalline grain boundaries behave qualitatively differently than those containing amorphous perovskite. The relatively high surface recombination velocity of $CH_3NH_3PbI_3$ (450 cm/s)[75] compared to our films (27 cm/s) suggests that grain boundaries will become a major source of losses in record solar cells once improvements in $CH_3NH_3PbI_3$ surface passivation are made.

To examine such effects, we model a solar cell and compute the maximum attainable photoluminescence quantum yield (PLQY) based on our film's characteristics (S_{GB} = 1670 cm/s, S_{FB} = 27 cm/s, L = 0.61 μm, and D = 0.18 cm^2/s, details in supplementary note 6). The solar cell

consists of a planar polycrystalline $CH_3NH_3PbBr_3$ absorber layer sandwiched between two transporting layers (TiO_2, and NiO_x) and metal contacts (FTO, and Au). Carrier transport is assumed to be isotropic; however, given recent reports on rapid carrier diffusion within grains[8,51], carrier transport within a perovskite thin film might be more accurately modeled anisotropically and therefore, our results can be considered an upper bound for the detrimental influence of grain boundaries. **Figure 4a** shows simulated *J-V* curves of solar cells with different grain sizes (homogeneous grain size for each). The grain size primarily regulates the open circuit voltage (V_{oc}), with minimal impact on the short-circuit current density (J_{sc}). If we assume a grain size distribution (as observed experimentally), then there is significant heterogeneity of the simulated local voltage of each individual grain. Since the full device can be modelled as a collection of individual grains connected electrically in parallel, the V_{oc} is limited by the smallest grains in this distribution[76]. For example when the width of the distribution is ~30% of the average grain size, the V_{oc} drops from ~1.5 V to ~1.33 V, precluding simple experimental device studies of the effect of grain size because samples with larger grain sizes also have wider distributions (inset in **Figure 4a**). Both the average and the distribution must be taken into account. This heterogeneity effect, however, is almost negligible if the device is stacked laterally resembling an interdigitated back contact solar cell[77]. In this regard, moving toward monocrystalline thin films for solar cells is still necessary for better device performance: completely removing grain boundaries from a 4 micron grain size halide perovskite film would increase V_{oc} by 110 mV (8%) in a solar cell with ideal contacts (67 mV increase in V_{oc} with simulated contact losses, **Figure 4a**). Clearly, minimizing the effects of grain boundaries is still required to improve the device performance.

Next, we simulated the photoluminescence quantum yield (PLQY) of our films by assuming that all losses at the grain boundary, on the front/back surface, and in the bulk contribute to monomolecular trap-assisted recombination. The analytical expression of equation 1 and 2 can be used to convert the minority carrier diffusion length into an effective lifetime that is inversely proportional to monomolecular recombination coefficient as a function of grain size (details in the supporting note 6). The carrier density required to reach a PLQY of 1% is reduced by one order of magnitude when we increase the grain size from 4 μm to 54 μm, and by two orders of magnitude when all grain boundaries are removed (monocrystalline film, **Figure 4b**). Having relatively large grain sizes up to 54 μm is still not enough to reach the monocrystalline

total integrated PLQY. We estimate that a half-millimeter grain size is required to get 96% of the monocrystalline performance, which is particularly important for 1 sun applications.

In conclusion, here we show the importance of using a true crystallographic measurement when studying the effect of grain boundaries in halide perovskite thin films. This is not only necessary for proper identification of grain boundaries but also enables deeper insights from studying dependence on misorientation angle, disorder at the interface, and heterogeneity in grain size. Using EBSD, we find that twinning does not play a role in the $CH_3NH_3PbBr_3$ films studied here, but the grain boundary recombination velocity of 1670 ± 50 cm/s plays a key role in lowering performance. Our modeling suggests that increasing the average grain size (and uniformity) to close to a millimeter or drastically lowering grain boundary recombination velocity is necessary to approach the limiting efficiency potential. Interestingly, under certain conditions amorphous regions can form at the grain boundaries, increasing photoluminescence intensity and lifetime without degrading carrier diffusion length. These results might explain the conflicting literature reports of grain boundary effects in halide perovskites: crystalline grain boundaries are detrimental to performance while amorphous regions can provide excellent passivation and longer lifetimes.

Competing financial interests

The EBSD detector used in this study is now being commercialized by Amsterdam Scientific Instruments.

Author contributions

ECG and SB conceived the idea. GWPA wrote the manuscript under the supervision of ECG, SB and DPF. HA and SB developed the controlled grain size deposition protocol. AL and GWPA carried out the electron back-scattered diffraction measurements and analysis. XL and YL carried out the synchrotron-based nanoprobe X-ray diffraction and analysis under the supervision of DPF. JDK carried out TOF-SIMS measurement and analysis under the supervision of SRE (the latter with SB). TD developed the photoluminescence lifetime fitting routine with SB. GWPA and SB designed and analysed the photoluminescence experiments, and GWPA conducted the photoluminescence and diffusion length measurements, developed the theoretical

modelling and built the steady-state photocarrier grating setup under the supervision of ECG. All authors discussed the results and reviewed the final manuscript.

Acknowledgments

The authors thank Dr. Bruno Ehrler and Dr. Aditya Mohite for giving feedback on the manuscript. ECG, AL, and GWPA thank Hans Poolman, Dmytro Byelov, Erik Maddox, and Dirk-Jan Spaanderman for fruitful discussions and support regarding the EBSD detector. GWPA thanks Luc Blom, Jan Zomerdijk, Erik Clay, Marnix Verweij, and Marc Duursma for their support in developing the SSPG setup, Dr. Sophie Meuret for helpful discussion on electron beam interactions with solids, Reinout Jaarsma and Johannes Kirschner for assistance with XPS measurements, Benjamin Daiber and Stefan Tabernig for help during the wide-field PL experiment, and Indra Sihar for helpful discussion on finite element analysis. SB and TD thank Dr. Forrest Bradbury for helpful discussions about the PL lifetime fitting routine. DPF, XL, and YL thank Martin Holt and Zhonghou Cai for supporting the nano-diffraction measurements, Shen Wang for assistance with FIB marker preparation, and the Hellman Foundation and the California Energy Commission (EPC-16-050) for financial support. This research used resources of the Advanced Photon Source, U.S. Department of Energy (DOE) Office of Science User Facility operated for the DOE Office of Science by Argonne National Laboratory under Contract No. DE-AC02-06CH11357. G.W.P.A was supported by TKI Urban Energy, "COMPASS" (TEID215022), at the end of this project. This work is part of The Netherlands Organization for Scientific Research (NWO). The work performed by Maastricht University was supported by the Dutch province of Limburg through the LINK programme. We acknowledge financial support from the European Research Council under the European Union's Seventh Framework Programme (FP/2007- 2013)/ERC Grant Agreement no. 337328, "NanoEnabledPV", and from an industrial partnership between Philips and FOM.

References

1 Wan-Jian Yina, T. S., and Yanfa Yan. Unusual defect physics in CH3NH3PbI3 perovskite solar cell absorber. *Appl.Phys.Lett* **104**, 4 (2014).

2 Aron Walsh, D. O. S., Shiyou Chen, X G Gong, and Su-Huai Wei. Self-Regulation Mechanism for Charged Point Defects in Hybrid Halide Perovskites. *Angew Chem Int Ed* **54**, 4 (2015).

3 Sung Heo, G. S., Yonghui Lee, Dongwook Lee, Minsu Seol, Jooho Lee, Jong-Bong Park, Ki Hong Kim, Dong-Jin Yun, Yongsu Kim, Jaikwang Shin, Tae Kyu Ahn and

Mohammad Khaja Nazeeruddin. Deep level trapped defect analysis in CH3NH3PbI3 perovskite solar cells by Deep Level Transient Spectroscopy. *Energy & Environmental Science*, doi:DOI: 10.1039/C7EE00303J (2017).

4 Guichuan Xing, N. M., Swee Sien Lim, Natalia Yantara, Xinfeng Liu, Dharani Sabba, Michael Grätzel, Subodh Mhaisalkar and Tze Chien Sum. Low-temperature solution-processed wavelength-tunable perovskites for lasing. *Nature Materials* **13**, 5 (2014).

5 Stranks, S. D. Nonradiative Losses in Metal Halide Perovskites. *ACS Energy Letters* **2**, 11, doi:10.1021/acsenergylett.7b00239 (2017).

6 D. Shi, V. A., R. Comin, M. Yuan, E. Alarousu, A. Buin, Y. Chen, S. Hoogland, A. Rothenberger, K. Katsiev, Y. Losovyj, X. Zhang, P.A. Dowben, O.F. Mohammed, E.H. Sargent, O.M. Bakr. Low trap-state density and long carrier diffusion in organolead trihalide perovskite single crystals. *Science* **347**, 4 (2015).

7 Jae S. Yun, A. H.-B., Shujuan Huang, Sang H. Woo, Yooun Heo, Jan Seidel, Fuzhi Huang, Yi-Bing Cheng, and Martin A. Green. Benefit of Grain Boundaries in Organic−Inorganic Halide Planar Perovskite Solar Cells. *J.Phys.Chem.Lett.* **6**, 6 (2015).

8 Dane W. deQuilettes, S. M. V., Samuel D. Stranks, Hirokazu Nagaoka, Giles E. Eperon, Mark E. Ziffer, Henry J. Snaith, David S. Ginger. Impact of microstructure on local carrier lifetime in perovskite solar cells. *Science*, 9 (2015).

9 Dae-Yong Son, J.-W. L., Yung Ji Choi, In-Hyuk Jang, Seonhee Lee, Pil J. Yoo, Hyunjung Shin, Namyoung Ahn, Mansoo Choi, Dongho Kim & Nam-Gyu Park. Self-formed grain boundary healing layer for highly efficient CH3NH3PbI3 perovskite solar cells. *Nature Energy* **1**, 8.

10 Obadiah G. Reid, M. Y., Nikos Kopidakis, Kai Zhu, and Garry Rumbles. Grain-Size-Limited Mobility in Methylammonium Lead Iodide Perovskite Thin Films. *ACS Energy Letters* **1**, 5 (2016).

11 Hyung Do Kim , H. O., Hiroaki Benten , and Shinzaburo Ito. Photovoltaic Performance of Perovskite Solar Cells with Different Grain Sizes. *Advanced Materials* **28**, 6 (2016).

12 Gede W. P. Adhyaksa, L. W. V., Yinghuan Kuang, Sarah Brittman, Ruud E. I. Schropp, and Erik C. Garnett. Carrier Diffusion Lengths in Hybrid Perovskites: Processing, Composition, Aging, and Surface Passivation Effects. *Chemistry of Materials* **28**, 5 (2016).

13 Mengjin Yang, Y. Z., Zhen Li, Dong Hoe Kim, Chun-Sheng Jiang, Jao van de Lagemaat and Kai Zhu. Do Grain Boundaries Dominate Non-Radiative Recombination in CH3NH3PbI3 Perovskite Thin Films? *Phys.Chem.Chem.Phys.* **19**, 8 (2017).

14 Dallas Fisher, F. S., Joon Jang, Tara P. Dhakal. The Effect of Grain Improvement on Carrier Lifetime in Perovskite Solar Devices. *Photovoltaic Specialists Conference (PVSC), 2016 IEEE 43rd*, 5 (2016).

15 Xiaodong Ren, Z. Y., Dong Yang, Xu Zhang, Dong Cui, Yucheng Liu, Qingbo Wei, Haibo Fana and Shengzhong (Frank) Liu. Modulating crystal grain size and optoelectronic properties of perovskite films for solar cells by reaction temperature. *Nanoscale* **8**, 7 (2016).

16 Wanyi Nie1, H. T., Reza Asadpour, Jean-Christophe Blancon, Amanda J. Neukirch, Gautam Gupta, Jared J. Crochet, Manish Chhowalla, Sergei Tretiak, Muhammad A. Alam, Hsing-Lin Wang, Aditya D. Mohite. High-efficiency solution-processed perovskite solar cells with millimeter-scale grains. *Science* **347**, 5 (2015).

17 Jun Haruyama, K. S., Liyuan Han, and Yoshitaka Tateyama. Termination Dependence of Tetragonal CH3NH3PbI3 Surfaces for Perovskite Solar Cells. *J. Phys. Chem. Lett.* **16**, 7 (2014).

18 T. Jesper Jacobsson, J.-P. C.-B., Elham Halvani Anaraki, Bertrand Philippe, Samuel D. Stranks, Marine E. F. Bouduban, Wolfgang Tress, Kurt Schenk, Joël Teuscher, Jacques-

E. Moser, Håkan Rensmo, and Anders Hagfeldt. Unreacted PbI2 as a Double-Edged Sword for Enhancing the Performance of Perovskite Solar Cells. *JACS* **138**, 13 (2016).

19 Qi Chen, H. Z., Tze-Bin Song, Song Luo, Ziruo Hong, Hsin-Sheng Duan, Letian Dou, Yongsheng Liu, and Yang Yang. Controllable Self-Induced Passivation of Hybrid Lead Iodide Perovskites toward High Performance Solar Cells. *Nano Letter* **14**, 6 (2014).

20 Giles E. Eperon, D. M., and David S. Ginger. Anticorrelation between Local Photoluminescence and Photocurrent Suggests Variability in Contact to Active Layer in Perovskite Solar Cells. *ACS Nano* **10**, 9 (2016).

21 Sibel Y. Leblebici, L. L., Yanbo Li, Sebastian E. Reyes-Lillo, Sebastian Wickenburg, Ed Wong, Jiye Lee, Mauro Melli, Dominik Ziegler, Daniel K. Angell, D. Frank Ogletree, Paul D. Ashby, Francesca M. Toma, Jeffrey B. Neaton, Ian D. Sharp and Alexander Weber-Bargioni. Facet-dependent photovoltaic efficiency variations in single grains of hybrid halide perovskite. *Nature Energy* **1** (2016).

22 Parisa Khoram, S. B., Wojciech I. Dzik, Joost N. H. Reek, and Erik C. Garnett. Growth and Characterization of PDMS-Stamped Halide Perovskite Single Microcrystals. *J.Phys.Chem.C*, 7 (2016).

23 Nadja Giesbrecht, J. S., Lukas Oesinghaus, Anreas Binek, Thomas Bein, Peter Müller-Buschbaum, and Pablo Docampo. Synthesis of Perfectly Oriented and Micrometer-Sized MAPbBr3 Perovskite Cyrstals for Thin-Film Photovoltaic Applications. *ACS Energy Letters* **1**, 5 (2016).

24 N.J. Jeon, J. H. N., Y.C. Kim, W.S. Yang, S. Ryu, S.I. Seok. Solvent engineering for high-performance inorganic-organic hybrid perovskite solar cells. *Nature Materials* **13**, 7 (2014).

25 Joseph S. Manser, M. I. S., Jeffrey A. Christians, Osman M. Bakr, and Prashant V. Kamat. Making and Breaking of Lead Halide Perovskites. *Acc.Chem.Res.* **49**, 9 (2016).

26 Yunlong Guo, K. S., Wataru Sato, Yutaka Matsuo, Kento Inoue, Koji Harano, Chao Liu, Hideyuki Tanaka, and Eiichi Nakamura. Chemical Pathways Connecting Lead(II) Iodide and Perovskite via Polymeric Plumbate(II) Fiber. *JACS* **137**, 8 (2015).

27 Yaoguang Rong, S. V., Rui Guo, Yanan Wang, Jiming Bao, Wenzhi Li, Zhiyong Fanc, and Yan Yao. Critical kinetic control of non-stoichiometric intermediate phase transformation for efficient perovskite solar cells. **8**, 8 (2016).

28 Jan Visser, B. v. d. H., S.J.A. Weijers, R. de Vries, J.L. Visschers. A GigabitpersecondRead-outsystemforMedipixQuads. *Nuclear Instruments and Methods in Physics Research A* **633**, 4 (2011).

29 X. Llopart, R. B., M. Campbell, L. Tlustos, W. Wong. Timepix, a 65k programmable pixel readout chip for arrival time, energy and/or photon counting measurements. *Nuclear Instruments and Methods in Physics Research A* **581**, 10 (2007).

30 E. Levine, W. L. B., and G. Thomas. Further Applications of Kikuchi Diffraction Patterns; Kikuchi Maps. *Journal of Applied Physics* **37**, 8 (1966).

31 Joshua J. Choi, X. Y., Zachariah M. Norman, Simon J. L. Billinge, and Jonathan S. Owen. Structure of Methylammonium Lead Iodide Within Mesoporous Titanium Dioxide: Active Material in High-Performance Perovskite Solar Cells. *Nano Letter* **14**, 7 (2014).

32 B.L. Adams, S. T. a., D. Kinderlehrer, I. Livshits, D.E. Mason, C-T. Wu, W.W. Mullins, G.S. Rohrer, A.D. Rollett, and D.M. Saylor. Extracting Grain Boundary and Surface Energy from Measurement of Triple Junction Geomtery. *Interface Science* **7**, 18 (1999).

33 W.T. Read, a. W. S. Dislocation Models of Crystal Grain Boundaries. *Physical Review* **78**, 15 (1950).

34 Y. Huang, a. F. J. H. Measurement of Grain Boundary Mobility During Recrystallization of A Single-Phase Aluminium Alloy. *Acta Mater.* **47**, 10 (1999).

35 Mitra Taheri, H. W., and Anthony Rollett. A Method of Measuring Stored Energy Macroscopically Using Statistically Stored Dislocations in Commercial Purity Aluminum *Metallurgical and Materials Transactions A* **37**, 7.
36 Daniel Abou-Ras, a. K. P. The impact of twinning on the local texture of chalcopyrite-type thin films. *Phys.Stat.Sol (RRL)* **5**, 3 (2007).
37 Jonathan D. Poplawsky, N. R. P., Chen Li , Chad M. Parish , Donovan Leonard , Yanfa Yan , and Stephen J. Pennycook. Direct Imaging of Cl- and Cu-Induced Short-Circuit Efficiency Changes in CdTe Solar Cells. *Advanced Energy Materials* **4**, 8 (2014).
38 Stokkan, G. Twinning in multicrystalline silicon for solar cells. *Journal of Crystal Growth* **384**, 7 (2013).
39 Robyn L. Woo, R. X., Yoji Kobayashi, Li Gao, Niti Goel, Mantu K. Hudait, Thomas E. Mallouk, and R. F. Hicks. Effect of Twinning on the Photoluminescence and Photoelectrochemical Properties of Indium Phosphide Nanowires Grown on Silicon (111). *Nano Letter* **8**, 6 (2008).
40 Evan Brown, C. S., Kohei Shimamura, Fuyuki Shimojo, and Aiichiro Nakano. Enhanced charge recombination due to surfaces and twin defects in GaAs nanostructures. *Journal of Applied Physics* **117**, 8 (2015).
41 Federica Bertolotti, L. P., Maksym V. Kovalenko, Sergii Yakunin, Antonio Cervellino, Simon J. L. Billinge, Maxwell W. Terban, Jan Skov Pedersen, Norberto Masciocchi, and Antonietta Guagliardi. Coherent Nanotwins and Dynamic Disorder in Cesium Lead Halide Perovskite Nanocrystals. *ACS Nano* **11**, 13 (2017).
42 Mathias Uller Rothmann, W. L., Ye Zhu, Udo Bach, Leone Spiccia, Joanne Etheridge, and Yi-Bing Cheng. Direct observation of intrinsic twin domains in tetragonal CH3NH3PbI3. *Nature Communication* **8**, 8 (2017).
43 Sergio Castellanos, K. E. E., Antoine Autruffe, Mallory A. Jensen, Ashley E. Morishige, Jasmin Hofstetter, Patricia Yen, Barry Lai, Gaute Stokkan, Carlos del Canizo, and Tonio Buonassisi. High-Performance and Traditional Multicrystalline Silicon: Comparing Gettering Responses and Lifetime-Limiting Defects. *IEEE Journal of Photovoltaics* **6**, 9 (2016).
44 David. P. Fenning, A. S. Z., Jasmin Hofstetter, Alexander Frey, Mariana I. Bertoni, Guso Hahn, and Tonio Buonassisi. Investigation of lifetime-limiting defects after high-temperature phosphorus diffusion in high-iron-content multicrystalline silicon. *IEEE Journal of Photovoltaics* **4**, 8 (2014).
45 M.I. Bertoni, S. H., B.K. Newman, D.P. Fenning, H.F.W. Dekkers, E. Carnagliotti, A. Zuschlag, G. Micard, G. Hahn, G. Coletti, B. Lai, and T. Bounassisi. Influence of defect type on hydrogen passivation efficacy in multicrystalline silicon solar cells. *Progress in Photovoltaics: Research and Applications* **19**, 5 (2010).
46 Y.M. Yang, A. Y., B. Hsu, W.C. Hsu, A. Yang, and C.W. Lan. Development of high-performance multicrystalline silicon for photovoltaic industry. *Progress in Photovoltaics: Research and Applications* **23**, 12 (2015).
47 Antoine Autruffe, V. S. H., Lars Arnberg, Marisa Di Sabatino. Dislocation generation at near-coincidence site lattice grain boundaries during silicon directional solidification. *Journal of Crystal Growth* **411**, 7 (2015).
48 G. Stokkan, S. R., O. Lohne, and W. Warta. Spatially resolved modeling of the combined effect of dislocations and grain boundaries on minority carrier lifetime in multicrystalline silicon. *Journal of Applied Physics* **101**, 9 (2007).
49 Isao Takahashi, N. U., Hiroshi Mizuseki, Yoshiyuki Kawazoe, Gaute Stokkan, and Kazuo Nakajima. Impact of type of crystal defects in multicrystalline Si on electrical properties and interaction with impurities. *Journal of Applied Physics* **109**, 5 (2011).
50 Dane W. deQuilettes, S. J., Sven Burke, Mark E. Ziffer, Jacob T.-W. Wang, Henry J. Snaith, and David S. Ginger. Tracking Photoexcited Carriers in Hybrid Perovskite

Semiconductors: Trap-Dominated Spatial Heterogeneity and Diffusion. *ACS Nano* **11**, 9 (2017).
51 Wenming Tian, R. C., Jing Leng, Junxue Liu, Yajuan Li, Chunyi Zhao, Jun Zhang, Weiqiao Deng, Tianquan Lian, Shengye Ji. Limiting Perovskite Solar Cell Performance by Heterogeneous Carrier Extraction. *Angew Chem Int Ed* **55**, 5 (2016).
52 Ryan J. Stoddard, F. T. E., John K. Katahara, and Hugh W. Hillhouse. Correlation between Photoluminescence and Carrier Transport and a Simple In Situ Passivation Method for High-Bandgap Hybrid Perovskites. *Journal of Physical Chemistry Letters* **8**, 10 (2017).
53 Leon W. Veldhuizen1 , G. W. P. A., Mirjam Theelen , Erik C. Garnett and Ruud E.I. Schropp. Benchmarking photoactive thin-film materials using a laser-induced steady-state photocarrier grating. *Progress in Photovoltaics* **25**, 9 (2017).
54 D. Ritter, E. Z., K. Weiser. Steady-state photocarrier grating technique for diffusion length measurement in photoconductive insulators. *Applied Physics Letters* **49**, 3 (1986).
55 I. Balberg, A. E. D., H.A. Weakliem. Self-consistency and self-sufficiency of the photocarrier grating technique. *Applied Physics Letters* **53**, 3 (1988).
56 N.C. Halder, a. T. R. W. Grain Boundary Effects in Polycrystalline Silicon Solar Cells. *Solar Cells* **8**, 23 (1983).
57 Dugas, J. 3D modelling of a reverse cell made with improved multicrystalline silicon wafers. *Solar Energy Materials and Solar Cells*, 18 (1994).
58 S. Banerjee, a. H. S. Grain boundary effects in polycrystalline silicon solar cells. *Solar cells*, 18 (1990).
59 Sproul, A. B. Dimensionless solution of the equation describing the effect of surface recombination on carrier decay in semiconductors. *J.Appl.Phys* **76**, 4 (1994).
60 G.E. Pike, a. C. H. S. The dc voltage dependence of semiconductor grain-boundary resistance. *J.Appl.Phys* **50**, 9 (1978).
61 Dinesh Prasad Joshi, a. D. P. B. Theory of Grain Boundary Recombination and Carrier Transport in Polycrystalline Silicon Under Optical Illumination. *IEEE Transaction of Electron Devices* **37**, 13 (1990).
62 Rolf Brendel, a. U. R. Effective diffusion lengths for minority carriers in solar cells as determined from internal quantum efficiency analysis. *J.Appl.Phys* **85**, 4 (1999).
63 S.M. Sze, a. K. K. N. *Physics of Semiconductor Devices*. (John Wiley & Sons, Inc, 2007).
64 Shockley, W. *Electron and Holes in Semiconductors*. (D.Van Nostrand Company, Inc., 1950).
65 Ye Yang, Y. Y., Mengjin Yang, Sukgeun Choi, Kai Zhu, Joseph M. Luther & Matthew C. Beard. Low surface recombination velocity in solution-grown CH3NH3PbBr3 perovskite single crystal. *Nature Communication*, 6 (2015).
66 B.G. Mendis, L. B., Q.Z. Jiang. A contactless method for measuring the recombination velocity of an individual grain boundary in thin-film photovoltaics. *AppPhysLett* **97**, 3 (2010).
67 J. Oualid, C. M. S., J. Dugas, J. P. Crest, and H. Amzil. Influence of illumination on the grain boundary recombination velocity in silicon. *J.Appl.Phys* **55**, 11 (1984).
68 Hang Cheong Sio, S. P. P., and Daniel Macdonald. Imaging Surface Recombination Velocities of Grain Boundaries in Multicrystalline Silicon Wafers via Photoluminescence. *Sol.RRL* **1**, 4 (2017).
69 Markus Gloeckler, J. R. S., and Wyatt K. Metzger. Grain-boundary recombination in Cu (In , Ga) Se 2 solar cells. *AppPhysLett* **98**, 10 (2005).
70 W.K. Metzger, I. L. R., M. Romero, P. Dippo, M. Contreras, R. Noufi, D. Levi. Recombination kinetics and stability in polycrystalline Cu(In,Ga)Se2 solar cells. *Thin Solid Films* **517**, 5 (2009).

71 Rui Sheng, A. H.-B., Shujuan Huang, Sheng Chen, Xiaoming Wen, Xiaojing Hao, and Martin A. Green. Methylammonium Lead Bromide Perovskite-Based Solar Cells by Vapor-Assisted Deposition. *JPCC* **7**, 5 (2015).
72 Ian L. Braly, D. W. d., Luis M. Pazos-Outon, Sven Burke, Mark E. Ziffer, David S. Ginger, and Hugh W. Hillhouse. Hybrid perovskite films approaching the radiative limit with over 90% photoluminescence quantum efficiency. *Nature Photonics* **12**, 7 (2018).
73 Roberto Brenes, D. G., Anna Osherov, Nikita K. Noel, Christopher Eames, Eline M. Hutter, Sandeep K. Pathak, Farnaz Niroui, Richard H. Friend, M. Saiful Islam, Henry J. Snaith, Vladimir Bulovic, Tom J. Savenije, and Samuel D. Stranks. Metal halide perovskite polycrystalline films exhibiting properties of single crystals. *Joule* **1**, 13 (2017).
74 Dane W. deQuilettes, S. K., Sven Burke, Rajan K. Paranji, Alfred J. Shropshire, Mark E. Ziffer, and David S. Ginger. Photoluminescence lifetime exceeding 8 micoseconds and quantum yields exceeding 30% in hybrid perovskite thin films by ligand passivation. *2016* **1**, 4 (2016).
75 Ye Yang, M. Y., David T. Moore, Yong Yan, Elisa M. Miller, Kai Zhu and Matthew C. Beard Top and bottom surfaces limit carrier lifetime in lead iodide perovskite films. *Nature Energy* **2**, 7 (2017).
76 Yude Su, C. L., Sarah Brittman, Jinyao Tang, Anthony Fu, Nikolay Kornienko, Qiao Kong & Peidong Yang. Single-nanowire photoelectrochemistry. *Nature Nanotech* **11**, 4 (2016).
77 Gede W. P. Adhyaksa, E. J., and Erik C. Garnett. Nanoscale Back Contact Perovskite Solar Cell Design for Improved Tandem Efficiency. *Nano Letter* **17**, 7 (2017).
78 B.W.Silverman. Kernel Density Estimation using the Fast Fourier Transform. *Journal of the Royal Statistical Society* **31**, 7 (1982).
79 Johannes M. Richter, M. A.-J., Aditya Sadhanala, Maxim Tabachnyk, Jasmine P. H. Rivett, Luis M. Pazos-Outon, Karl C. Godel, Michael Price, Felix Deschler, and Richard H. Friend. Enhancing photoluminescence yields in lead halide perovskites by photon recycling and light out-coupling. *Nature Communication*, 8 (2016).
80 Ye Yang, M. Y., Zhen Li, Ryan Crisp, Kai Zhu, and Matthew C. Beard. Comparison of Recombination Dynamics in CH3NH3PbBr3 and CH3NH3PbI3 Perovskite Films: Influence of Exciton Binding Energy. *J. Phys. Chem. Lett.* **6**, 5 (2015).

Figures

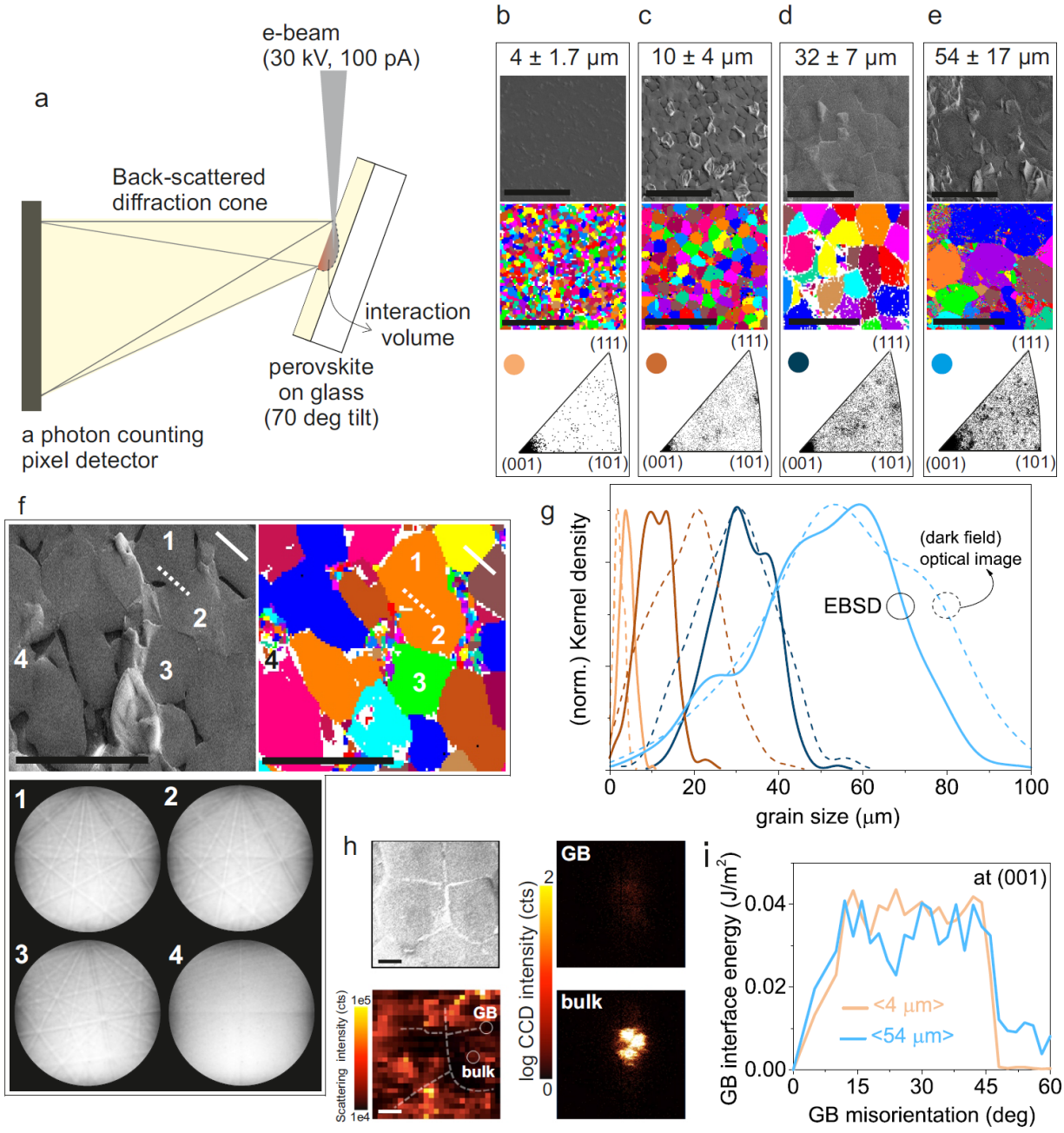

Figure 1. Electron back-scattered diffraction (EBSD) maps of $CH_3NH_3PbBr_3$ perovskite films with different grain sizes. (a) Schematic of our EBSD measurement. Collection of scanning electron-microscope (SEM) image (top panel) with its corresponding EBSD grain maps (middle panel), and distribution plot of crystallographic orientations (bottom panel) of perovskite films with 4 ± 1.7 μm **(b)**, 10 ± 4 μm **(c)**, 32 ± 7 μm **(d)**, and 54 ± 17 μm **(e)** grain sizes. The EBSD maps for 32 ± 7 μm grain size show disordered regions near the grain boundary (featured

as a white colour). The color maps do not represent the actual crystallographic orientation. **(f)** Deceiving features of grain boundaries showing two contrasting cases where the boundary that is visible under SEM (top left panel; indicated by the white dashed line) is not an actual grain boundary from the EBSD (see the corresponding EBSD maps; top right panel); whereas within the apparent smooth grain under SEM (top left panel; indicated by the white line), there is an invisible grain boundary (top right panel; see the different colour maps under the EBSD). The bottom panel shows Kikuchi bands obtained by averaging multiple diffraction patterns per pixel within one scanning area (~200 – 600 pixels). The scanning areas **1** and **2** show identical Kikuchi bands, and this pattern is different than that of scanning area **3**. Scanning area **4** shows no distinct backscattered diffraction. All scale bars are 50 μm. **(g)** Kernel density distribution of the grain size statistic (with a bandwidth of h = 0.337)[78] obtained from the EBSD compared with dark-field optical images. The size of the grains obtained from the optical images can be misleading (by a factor of up to 1.9). **(h)** Top left: SEM image of grain boundary region. Bottom left: Summed scattering intensity across the (002) $MAPbBr_3$ peak when rocking θ=12.86°, 13.47°, and 14.07° with 2θ fixed at 26.94°. The dashed lines are guides to the eye. Scale bars are 4 um. Top right: Diffraction pattern at the ”GB” point highlighted in the scattering intensity map (bottom left). Bottom right: diffraction pattern at the “Bulk” point highlighted in the scattering intensity map. Scale bars 3 mrad. Neither intermediate nor $PbBr_2$ phases were detected along the grain boundaries (**Figure S11**). **(i)** Grain boundary surface energy as a function of grain boundary misorientation for (001) crystal orientation and two grain sizes.

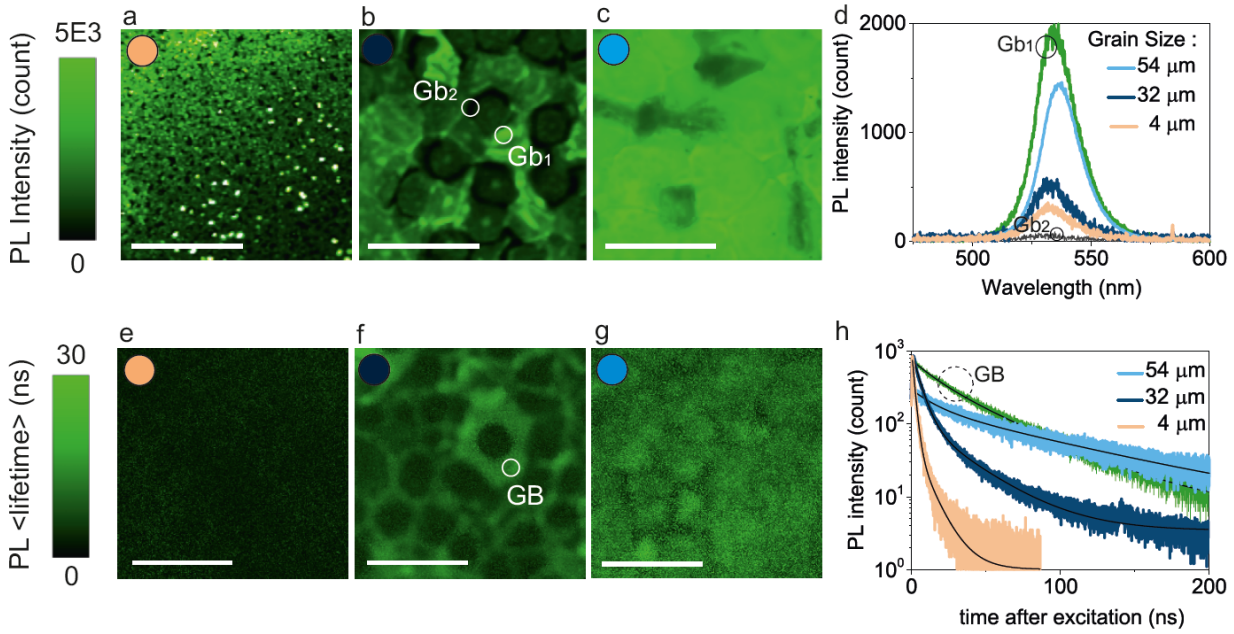

Figure 2. Photoluminescence (PL) intensity and lifetime of $CH_3NH_3PbBr_3$ perovskite films with different grain sizes. PL intensity maps with 4 ± 1.7 μm **(a)**, 32 ± 7 μm **(b)**, and 54 ± 17 μm **(c)** grain sizes showing local heterogeneity is more pronounced near the apparent grain boundary for the <32 μm>-grain sample**. (d)** PL spectra showing a similar emission wavelength regardless of the grain sizes; the difference of PL intensity at around the apparent grain boundary for the <32 μm> grain is highlighted (spot Gb1 and spot Gb2). PL effective lifetime maps (integrating time-trace decay that is a convolution of trap-assisted, radiative, and Auger recombination processes) with 4 ± 1.7 μm **(e)**, 32 ± 7 μm **(f)**, and 54 ± 17 μm **(g)** grain sizes**. (h)** Time-resolved PL decay traces showing a faster PL decay for samples with smaller grain sizes. For the sample with medium-sized grains, the PL lifetime near the apparent grain boundary always exhibits a slower decay (spot GB) as compared to its grain interior. The recombination coefficients are extracted by fitting the PL decay traces (black lines). All scale bars (Figure 3a-c, and e-g) are 50 μm.

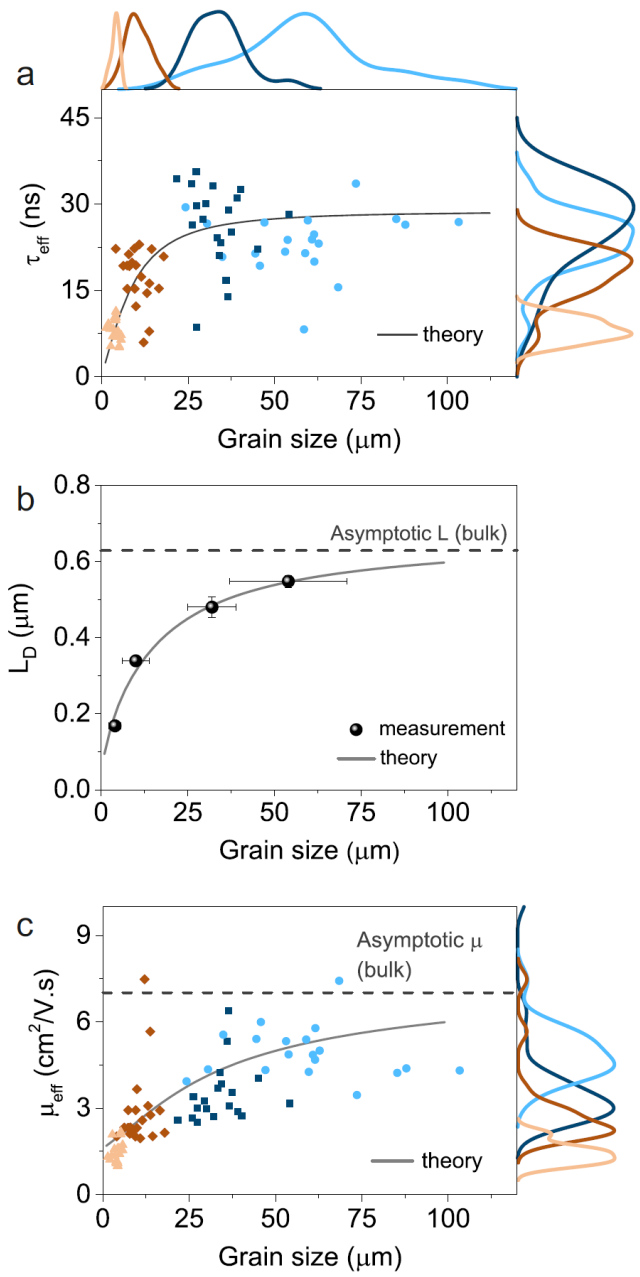

Figure 3. Statistical correlation of grain sizes and optoelectronic properties of $CH_3NH_3PbBr_3$ perovskite. (a) The effective carrier lifetimes (τ_{eff}) *versus* grain sizes. The τ_{eff} is extracted from the PL decay traces where each point represents an area mapping of 80 μm · 80 μm size within the same substrate; right y-axis: the kernel distribution (with a bandwidth of h = 0.337)[78] is to illustrate the distributions of the extracted τ_{eff}; top x-axis: distributions of grain sizes from EBSD (identical to **Figure 1g**). **(b)** minority carrier diffusion length (L_D) *versus* grain size; the L_D values are extracted from steady-state photo-carrier grating measurements (SSPG) across scanning areas of ~0.5 cm · 0.5 cm; the *y*-error bars represent linear propagation of error from the measurement, while *x*-error bars represent a 95% confidence interval. **(c)** carrier mobility (μ_{eff}) versus grain size; the data is calculated from each data point of τ_{eff} (**Figure 3a**) and the L_D values (**Figure 3b**). All measurements were conducted on identical samples with nearly the same spot area.

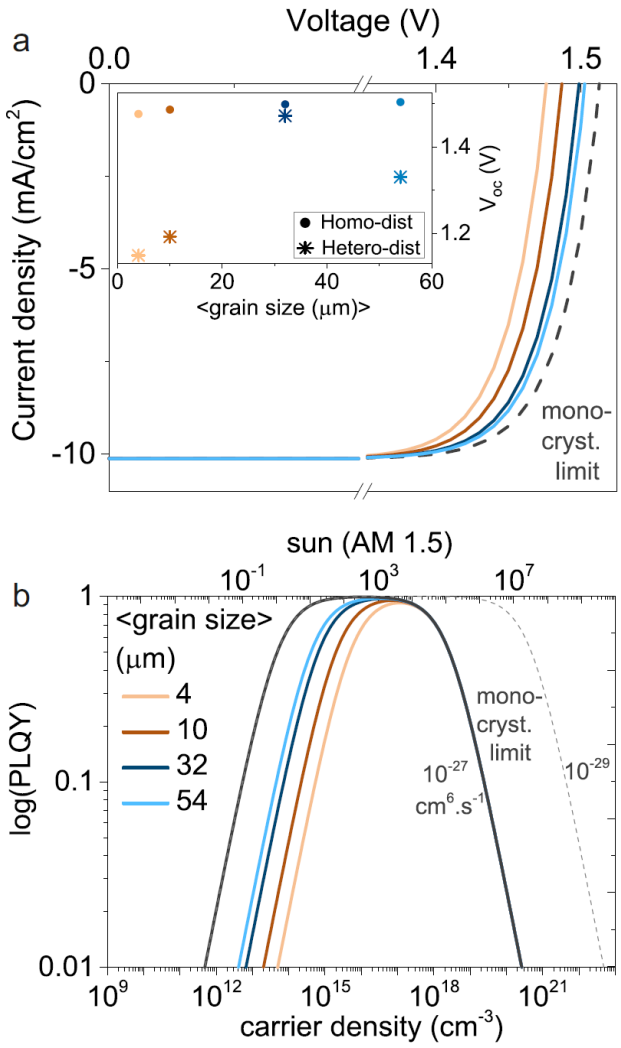

Figure 4. Modelling the characteristics of solar cells and photoluminescence quantum yield with different grain sizes of $CH_3NH_3PbBr_3$ perovskite. (a) simulated *I-V* curve showing that larger grain size increases V_{oc}. This correlation becomes randomized when the heterogeneity of grain size (the experimental standard deviation) is introduced into the model (the inset). Colors have the same labels in both panels. **(b)** Simulated PLQY as a function of the carrier density for different grain sizes using experimentally determined parameters; the PLQY at higher fluence is mainly limited by Auger recombination with two limiting values chosen from the literature[79,80].